Journal of Aerosol Science 183 (2025) 106478

Contents lists available at ScienceDirect

Journal of Aerosol Science

journal homepage: www.elsevier.com/locate/jaerosci

Computational and experimental investigation of an aerosol extraction device for use in dentistry

Vahid Goodarzi Ardakani [a], Mojtaba Dorri [b], Bin Zang [c], Angela H. Nobbs [d], Stephen Cross [e], Alberto M. Gambaruto [f,*]

[a] School of Electrical, Electronic and Mechanical Engineering, University of Bristol, Bristol BS8 1TH, UK
[b] University Hospitals Bristol and Weston NHS Foundation Trust, Bristol Dental Hospital, Lower Maudlin Street, Bristol BS1 2LY, UK
[c] School of Civil, Aerospace and Design Engineering, University of Bristol, Bristol BS8 1TH, UK
[d] Bristol Dental School Research Laboratories, Dorothy Hodgkin Building, Whitson Street, Bristol BS1 3NY, UK
[e] Wolfson Bioimaging Facility, Faculty of Health & Life Sciences, Biomedical Sciences Building, University of Bristol, University Walk, Bristol BS8 1TD, UK
[f] School of Engineering Mathematics and Technology, University of Bristol, Bristol BS8 1TH, UK

ARTICLE INFO

Editor: Dr. Chris Hogan

Keywords:
Infection transmission
Dentistry
Protective device
Numerical simulations
Experimental evaluation
Aerosol generating procedures

ABSTRACT

Medical procedures carry a high risk of pathogen transmission from patients to healthcare providers, the clinic environment, and subsequent patients. While measures such as patient mask wearing can help to reduce this danger, they may not always be possible, especially in dental treatments that need access to patients' airways. A protective device was designed and built to effectively confine airborne particles during medical procedures without interfering with medical operations. The device is evaluated and its working principles discussed.

The device resembles a dome and comprises of four primary mechanisms to inhibit the spread of potentially infected aerosols during aerosol-generating procedures (AGPs) in dental surgery: (i) a physical barrier; (ii) air curtains; (iii) an extraction point; (iv) a sustained airflow ingress. Evaluation is carried out using experiments in laboratory and clinical settings, as well as high-resolution numerical simulations.

Results of the numerical simulations of the prototype device show over 99% capture in its design configuration. The results from experiments also report high efficiency. A detailed analysis of the device and recommendations for future development are provided. The results from tests in the clinical setting will be provided in detail in another paper.

1. Introduction

Airborne transmitted diseases have garnered recent widespread interest within healthcare systems, particularly with the recent advent of the severe acute respiratory syndrome coronavirus 2 (SARS-CoV-2), which caused a pandemic outbreak and affected the mortality rate of the global population. Indeed, some airborne aerosols are biologically active as carriers of pathogens, such as viruses, bacteria and fungal spores, which may pose a significant threat to public health. These are present as droplets or particulates suspended in air that risk being inhaled, but also as deposited fomites on surfaces. The global adverse impacts of the SARS-CoV-2 virus underscore the need for continued research in the field of particle transport in indoor spaces and its interaction with the human respiratory system to minimise airborne outbreak transmission, with numerical modelling and simulations contributing significantly

* Corresponding author.
E-mail address: alberto.gambaruto@bristol.ac.uk (A.M. Gambaruto).

https://doi.org/10.1016/j.jaerosci.2024.106478
Received 19 July 2024; Received in revised form 12 October 2024; Accepted 14 October 2024
Available online 28 October 2024

to this research (Feng, Marchal, Sperry, & Yi, 2020; Mariam et al., 2021; Mutuku, Hou, & Chen, 2020; Setti et al., 2020; Talaat, Abuhegazy, Mahfoze, Anderoglu, & Poroseva, 2021).

During inhalation, one of the principal functions of the upper airways is to filter harmful particles from the ambient air. The upper airways protect the delicate pulmonary structures deep in the respiratory system from diseases and inflammation caused by deposited inhaled particles in the human respiratory tract (Doorly, Taylor, & Schroter, 2008). The World Health Organization (WHO) has presented a threshold classification for particles carrying pathogens, specifying that particles of a diameter ranging from 5 μm and above may carry pathogens and lead to infection transmission (Organization et al., 2014). Recent guidelines specifically related to SARS-CoV-2 indicate that respiratory droplet transmission involves particles of 5 – 10 μm and can occur when a person is in close contact (within 1 m) with an infected person who has respiratory symptoms or who is talking or singing (Organization, 2020). Recent literature examining deposition models, however, has revealed that particles larger than 10 μm are inclined to be deposited in the upper airway, while particles smaller in size are more likely to traverse into the lower respiratory tract to some degree (Gralton, Tovey, McLaws, & Rawlinson, 2011). The latter case is recognised as a more life-threatening health hazard and should be prioritised for aerosolized respiratory transmission measures. In dentistry, aerosols typically refer to droplets less than 50 μm in diameter, with those smaller than 10 μm considered an inhalation risk (Sergis et al., 2021). Recent studies focused on transmission in the dentistry setting when Aerosol Generating Procedures (AGPs) are involved, suggest that larger aerosols (>5 μm) will tend to have a limited travel range and typically within 1 m, while smaller aerosols (<0.3 μm) will remain at elevated levels if there is no active aerosol-management intervention (Ehtezazi et al., 2021; Innes et al., 2021). Droplet nuclei (≤5 μm in diameter) can remain suspended in air for many hours and be moved by air currents (Ehtezazi et al., 2021). The upshot of these considerations led us to focus on monodispersed 10 μm particles for the size range identified, since these will constitute an inhalation risk and will be challenging to redirect with airflow due to their high momentum at the instance of their generation. In general, aerosols are spread whenever infected individuals engage in respiratory activities such as breathing, sneezing, talking and coughing, generating particle droplets between 0.05 and 500 μm in open-air spaces (Gralton et al., 2011). Recent studies of aerosol transport during coughing have identified evaporation as a key factor in the range of transmission, since evaporation can occur in brief time periods and greatly affect the size of the aerosols (Calmet et al., 2021; Liu, Wei, Li, & Ooi, 2017).

Of particular interest is the transmission in healthcare settings, and it is crucial to diminish the prevalence of hazardous respiratory pathogens in each route of transmission in the healthcare community and the general population (Calmet et al., 2022; Perella, Tabarra, Hataysal, Pournasr, & Renfrew, 2021). Numerous medical and surgical procedures fall under the category of AGPs, exposing healthcare providers in close proximity with potentially infectious aerosols and thereby elevating the risk to their safety. In response to the SARS-CoV-2 (COVID-19) pandemic, extensive research efforts have been dedicated to devising strategies for containing and mitigating potentially contaminated aerosols during AGPs. One such approach involves the utilisation of barrier enclosure devices (Lyaker, Al-Qudsi, & Kopanczyk, 2020; Ong et al., 2022; Pirker, Čebašek, Serdinšek, & Remškar, 2021; Price, Ben-Yakov, Choi, Orchanian-Cheff, & Tawadrous, 2021). These devices can be broadly categorised into physical barriers, including boxes and plastic sheets, both with and without frames that, depending on their application, can be complemented by negative suction systems (Matava, Yu, & Denning, 2020; Phu et al., 2020; Price et al., 2021). An aerosol extraction device for applications of surgical tracheotomy, in which the ejection of aerosols is modelled as a focused jet, similarly comprises of a physical barrier and a suction mechanism, with the most effective location of the suction being directly above the patient based on the jet directivity (Calmet et al., 2022).

Dental practitioners face exposure to transmission via emitted sprays, including aerosols and splatter generated during dental procedures. Even a routine oral examination involving the use of air spray qualifies as an AGP. This significantly heightens the risks of airborne transmitted diseases for dental practitioners. During the COVID-19 pandemic, due to the absence of a suitable protective device, global dental care substantially moved towards the crucial therapy of acute conditions with a focus on exodontia, as well as guidance, analgesics, and antibiotics when pain relief is insufficient. The intricacy of dental sprays highlights the difficulties that the dentistry field has, as well as the risks posed to individuals. This emphasises the pressing need for protective devices capable of containing and extracting contaminants while performing operations. In response, a portable device was designed and tested to reduce exposure for dental practitioners, with the key findings reported in the present study.

The present study details a recently developed device to contain aerosols generated in a dentistry setting, reducing exposure and potential transmission of infection. The investigation comprises of experimental, numerical and clinical testing. The numerical simulations provide high resolution data, serving as an important tool to guide the design process and perform critical evaluation of the device's performance. The detailed analysis of the device, its components and their combined function, offers a basis and guide for the development of further devices with similar applications. The aim it to devise protective devices that can be employed regularly in clinical settings, to reduce the transmission routes, with the foreseeable impact to reduce the spread of infections. The device studied is covered by patents in the UK and internationally.

The paper is organised as follows. In Section 2 the computational and experimental considerations are presented. In particular, in Section 2.1 the reasoning behind the device design is detailed, providing a structured description of the various key components. This is followed in Section 2.2 with a one-dimensional analytical solution of particle motion in counter flow, to provide an estimate and justification of the choice of the air curtain flow speed. The governing equation to the fluid mechanics and particle transport are provided respectively in Sections 2.3 and 2.4, while the details of the numerical schemes, model setup and boundary conditions are given in Section 2.5. The various cases investigated numerically are detailed in Section 2.6, while the experimental setup in clinical and laboratory settings are provided respectively in Sections 2.7 and 2.8. The results are given in Section 3, first presenting the experimental results followed by those of the computational investigation in greater depth. The discussion is then given in Sections Section 4 and finally the conclusions in Section 5.

2. Materials and methods

A dome-shaped device was designed to contain aerosols generated during dental procedures, intended to reduce potential transmission risks in healthcare settings. The efficacy of the device was assessed using experiments in laboratory and clinical settings, as well as numerical simulations with several case scenarios investigated. These complementary techniques allowed for a thorough evaluation of the ability of the device to eliminate particles during AGPs.

Different views of the device and the relevant dimensions are shown in Fig. 1. The setup in the clinical bay and the computational domain for the numerical simulations are shown in Fig. 2.

2.1. The device design, components and function

The device resembles a dome and comprises of four primary mechanisms to inhibit the spread of potentially infected aerosols during AGPs in dental surgery: (i) the dome-shaped device, which acts as a physical barrier; (ii) air curtains, formed using a set of jets positioned around the side openings in the device wall that allow direct access to the patient, effectively sealing these openings; (iii) an extraction point, which removes and processes the air as well as maintains ventilation; (iv) a low momentum airflow through the side openings, to ensure flow is directed to the extraction point.

The dome serves as the physical barrier and defines the interior space of the device, accommodating the patient's head. Given that the patient's head may be inclined at various angles, and high momentum aerosols formed through AGPs are ejected in various directions, a physical barrier is the only sure approach to ensure the aerosols are captured and contained. A physical barrier does not allow flow or aerosols to traverse, making it particularly effective when large variability and unknown factors are present.

The device features two access side openings designed as access points across the dome, enabling medical practitioners to reach unhindered the interior of the dome to conduct procedures in their usual approach. A set of jets is positioned around the perimeter of each side opening and are configured to direct airflow across the side openings to generate air curtains. The air curtains act as a traversable seal and this design effectively reduces the transmission of airborne aerosols through these openings. The side openings are referred to as *left* or *right* opening, in relation to the patient's orientation.

The device is equipped with a suction hole to extract air from the interior space of the dome, located approximately centrally on the dome and in front of the patient. An aerosol extraction device for applications of surgical tracheotomy is similarly equipped with a suction mechanism, with the suction directly above the patient (Calmet et al., 2022). The suction flow rate should be greater than the sum flow rate of the air curtains and respiration, in order to ensure the air, once it has entered the dome and has potentially become contaminated, flows out solely through the suction hole. This results in a constant low momentum airflow ingress through the side openings.

The device also comprises of two manifolds to supply the flow to the air curtain: the internal manifold, which is attached to the dome, and the external manifold, which is linked to an air pump source. The jet nozzles, which form the air curtain, are protruded from the internal manifold. A thin porous layer with the thickness of 1 mm lies in between the internal and external manifolds, facilitating the uniform distribution of air to the jets.

The prototype design, as shown in Fig. 1, comprises of: the suction hole with a diameter of 15 cm, the inlet of the manifold measures 5.8 cm in diameter, the dome itself has a radius of 30 cm. Each access side opening is designed with wider dimensions horizontally than vertically, resulting in an approximate area of 0.061 m^2. Surrounding each side opening are: 23 jet holes along the bottom, 19 along the top, and 11 along both the left and right sides. These jet holes each have a diameter of 8 mm.

2.2. Prototype design of the device

In order to estimate appropriate design parameters, such as the flow speed of the air curtain and dimension of the dome, one would wish to calculate the maximum distance a particle would travel, aiming not to exceed the dome barrier. To obtain this estimate of distance travelled, let us assume that a head-on air flow is present, Stokes' drag law is an accurate description of the force acting on a spherical aerosol (hence low particle Reynolds number), and that drag is the sole force at play, leading to an equation of motion of the aerosol, which is one-dimensional and given by

$$m_p \frac{d^2 x_p}{dt^2} = 6\mu\pi r \left(v_f - \frac{dx_p}{dt} \right) \tag{1}$$

where μ is the fluid dynamic viscosity, m_p is the mass of the particle, r is the particle radius, v_f is the constant fluid velocity, and x_p is the particle position. The solution to this second-order linear ordinary differential equation is

$$x_p(t) = v_f\ t + c_1 \frac{e^{-At}}{A} + c_2 \tag{2}$$

where $A = 6\mu\pi r/m_p$, and c_1, c_2 are constants of integration. Taking initial conditions of $x_p(t=0) = 0$ and $u_p(t=0) = u_0$, we rewrite the solution as

$$x_p(t) = v_f\ t + \frac{v_f - u_0}{A} e^{-At} + \frac{u_0 - v_f}{A} \tag{3}$$

from which the particle speed is readily found to be

$$u_p(t) = \frac{dx_p}{dt} = v_f - (v_f - u_0) e^{-At} \tag{4}$$

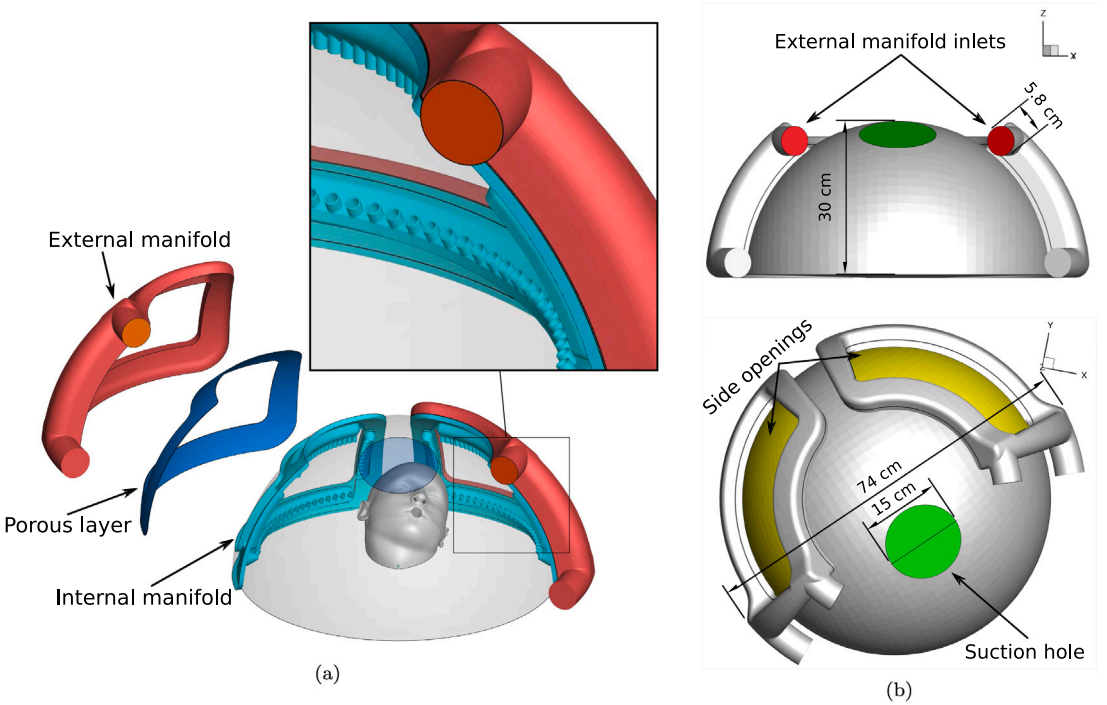

Fig. 1. Detail of shield components, deconstructed on left hand side and assembled on right hand side. (a) Components include: the external manifold (red), the porous layer (blue) and the internal manifolds with jet outlet pointing into the dome (cyan). (b) Key dimensions of the shield are presented, and boundaries are identified as: the suction hole (green), the inlets of external manifold (red) and the access side openings (yellow). The diameter of mouth and nostrils in this setup were considered to be 2 cm and 0.8 cm, respectively. (For interpretation of the references to colour in this figure legend, the reader is referred to the web version of this article.)

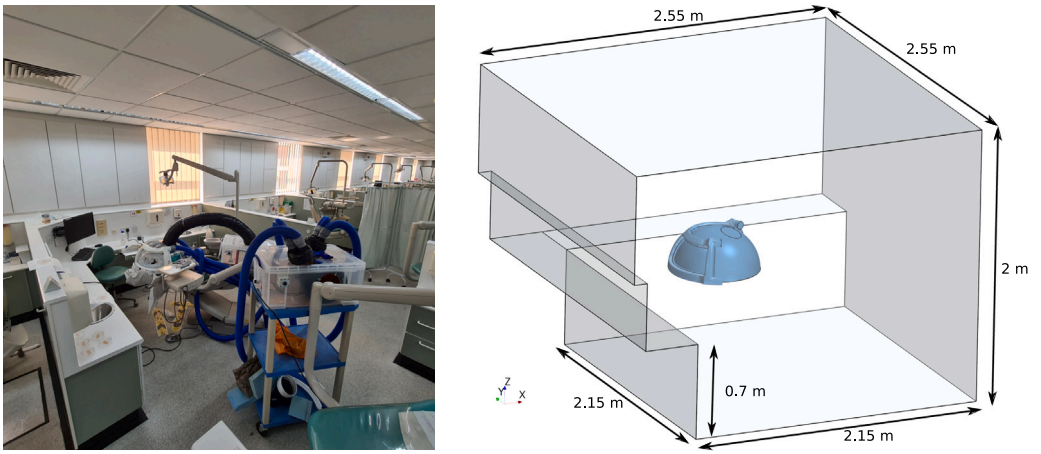

Fig. 2. (Left) Location of the device with the ventilation system set up within a clinical bay. (Right) the virtual model retaining key features of this setup.

On computing the maximum distance travelled by the particle into the head-on air flow before it reverses, we find that the time taken to arrive to $u_p(t) = 0$ is

$$t_{u_p=0} = \frac{1}{A} \ln\left(1 - \frac{u_0}{v_f}\right) \tag{5}$$

and consequently the distance travelled in this time is

$$x_{u_p=0} = \frac{1}{A}\left(v_f \ln\left(1 - \frac{u_0}{v_f}\right) + u_0\right) \tag{6}$$

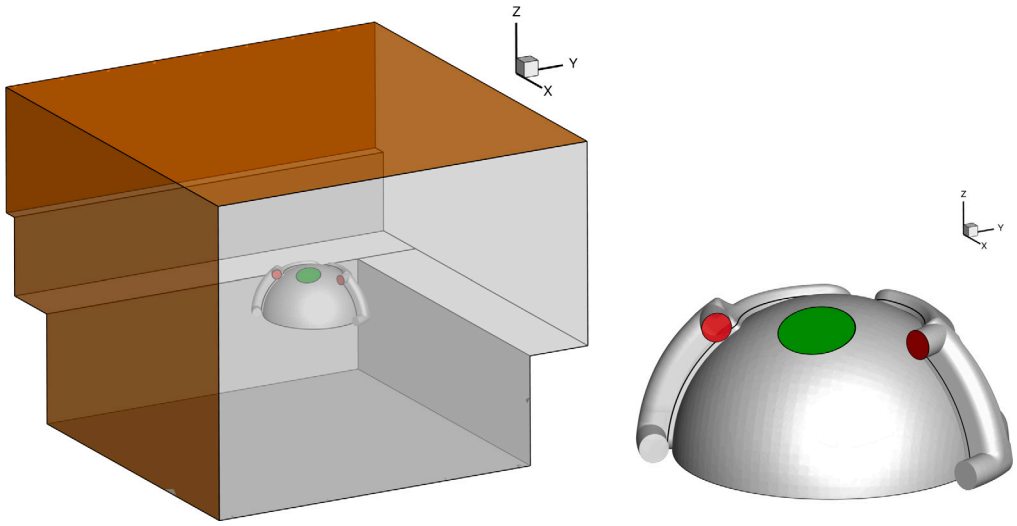

Fig. 3. (Left) Computational domain of the clinical bay and the device. The boundary conditions of the room are presented, where the artificial boundaries are shaded orange and are modelled as a pressure outlet boundary condition, while the dark grey boundaries represent solid objects and are modelled as a no-slip boundary condition. (Right) The manifold inlets are shaded red while the suction hole outflow is shaded green. (For interpretation of the references to colour in this figure legend, the reader is referred to the web version of this article.)

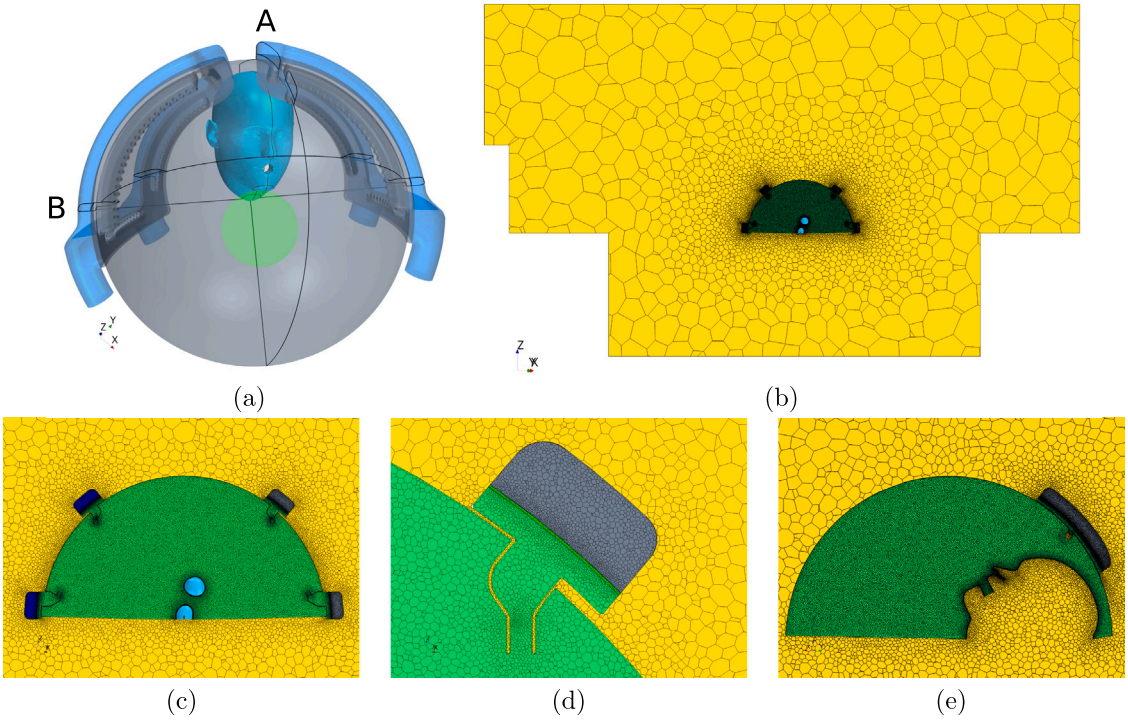

Fig. 4. Detail of the computational mesh in different subregions of the domain. (a) 3D view of the dome and patient's head; (b) cross-section B across the room and dome; (c) detailed view of the dome space on cross-section B; (d) detailed view of the manifold and nozzle; (e) distribution of the mesh on cross-section A.

Taking $r = 5 \times 10^{-6}$ m (hence 10 μm diameter aerosol), $\mu = 1.855 \times 10^{-5}$ Pa s, $m_p = 5.2 \times 10^{-13}$ kg, $u_0 = 400$ m s^{-1} and $v_f = -8$ m s^{-1}, we find $x_{u_p} \approx 0.1$ m and $t_{u_p} \approx 0.001$ s The air speed v_f is identified from the available experimental setup, while the aerosol initial speed u_0 is based on typical burr handpiece performance from Sergis et al. (2021) as a worst case scenario, as described further in Section 2.5. It is worth noting that from the expressions for the maximum distance and time of travel before

the aerosol reverses, given by Eqs. (5) and (6) and rewriting $1/A = m_p/6\mu\pi r = 2\rho_p r^2/9\mu$ where ρ_p is the density of the aerosol, we find the aerosol radius has a quadratic influence. Consequently, variations in the aerosol radius will have a greater influence on the dynamics in comparison to other parameters.

The dome radius was consequently chosen to be $R = 0.3$ m, being considerably greater than the stipulated aerosol arrest distance of $x_{u_p} \approx 0.1$ m, with additional considerations of patient comfort and clinician access. The design was based on feedback from an Advisory Group of healthcare professionals who were provided with the questions reported in the Appendix and some conceptual designs.

The prototype design was developed in collaboration with Ingenia Industrial Design LLP (0000a) and STL-Tech (0000b) for the CSD development, and fabricated in perspex. The mannequin employed for the experimental tests is a standard model used in dentistry. The head model employed in the numerical simulations is a representative CAD model.

2.3. Governing equations for the fluid dynamics

The governing equations for the fluid dynamics comprise of the continuity and Navier–Stokes equations, which respectively express the conservation of mass and linear momentum. Suitably assuming a constant density and viscosity of the air, these are given by

$$\nabla \cdot \boldsymbol{u} = 0 \tag{7}$$

$$\frac{\partial \boldsymbol{u}}{\partial t} + (\boldsymbol{u} \cdot \nabla)\boldsymbol{u} = -\frac{\nabla p}{\rho} + \nu \nabla^2 \boldsymbol{u} + \boldsymbol{g} \tag{8}$$

where $\nu = 1.57 \times 10^{-5}$ m^2 s^{-1} is the kinematic viscosity, $\rho = 1.184$ kg m^{-3} is the density, p is the pressure, $\boldsymbol{u}$ is the velocity of the flow, and $\boldsymbol{g} = 9.81$ m s^{-2} is the acceleration due to gravity. The dynamic viscosity is therefore $\mu = 1.855 \times 10^{-5}$ Pa s.

The porous layer, placed between the external and internal manifolds, generates a homogeneous pressure field upstream of the jets, leading to an approximately equal flow rate distribution at the jet outlets and hence an evenly distributed air curtain. The effect of the porous layer in the equations can be modelled through a source term within the momentum equation. The continuity and momentum equations that are solved in porous layers are hence respectively given by

$$\frac{\partial(\varepsilon\rho)}{\partial t} + \nabla \cdot (\rho \boldsymbol{u}_s) = 0 \tag{9}$$

$$\rho \frac{\partial \boldsymbol{u}_s}{\partial t} + \rho(\boldsymbol{u}_s \cdot \nabla)\boldsymbol{u}_s = -\nabla P + \mu \nabla^2 \boldsymbol{u}_s + \boldsymbol{f}_b + \boldsymbol{f}_p \tag{10}$$

where $\varepsilon = V_f/V_v$ is the porosity, which is defined as the ratio of fluid volume (V_f) to the total volume (V_v). The term $\boldsymbol{f}_b$ represents all the body forces acting on the fluid except the porous resistance, and $\boldsymbol{f}_p$ denotes the porous resistance force (CD-adapco, 2017). In Eq. (10), the term $\boldsymbol{u}_s = \varepsilon \boldsymbol{u}$, referred to as the *superficial velocity*, is defined as the volume flow rate through a unit cross-sectional area of the domain, which includes both solid and fluid regions (Goodarzi Ardakani, 2023). The porous resistance force $\boldsymbol{f}_p$ is given by

$$\boldsymbol{f}_p = -\mathbf{P} \cdot \boldsymbol{u}_s \tag{11}$$

where $\mathbf{P}$ is the porous resistance tensor, which comprises two components

$$\mathbf{P} = \mathbf{P}_v + \mathbf{P}_i |\boldsymbol{u}_s| \tag{12}$$

where $\mathbf{P}_v$ and $\mathbf{P}_i$ are viscous and inertial resistance tensors, respectively. We consider the porous medium to be composed of a homogeneous and isotropic material, resulting in isotropic resistance tensors. The isotropic viscous resistance was set to be 10^4 kg m^{-3} s^{-1} and the inertial resistance was set to 10^4 kg m^{-4}. These values are representative only and ensure the air curtain jet velocities are approximately uniform as evidenced by the experimental analysis.

2.4. Governing equations for the passive scalar and particle transport

A passive scalar is introduced at the inlet boundaries to track and observe the flow evolution, facilitating a visual analysis of the fluid dynamics. The passive scalar has matching properties to the fluid and is transported by the fluid. The dynamics of the passive scalar field can therefore be described by the advection–diffusion equation, given by

$$\frac{\partial \phi}{\partial t} + \nabla(\boldsymbol{u}\,\phi) = D\nabla^2 \phi \tag{13}$$

where ϕ refers to the concentration of the scalar with permissible range $\phi = [0, 1]$ (Ardakani et al., 2023). The effective diffusivity, D, combines molecular and turbulent diffusivity, and is defined as

$$D = \frac{\mu}{\rho\, Sc} + \frac{\mu_t}{\rho\, Sc_t} \tag{14}$$

where μ and μ_t are the fluid dynamic viscosity and turbulent viscosity, respectively, with μ_t computed during the simulation (Menter, 1994). The dimensionless coefficients $Sc = 900$ and $Sc_t = 0.9$ are the passive scalar molecular Schmidt number and turbulent Schmidt number. While the value of the Schmidt number for air is $Sc \approx 0.6$, the higher value of $Sc = 900$ was employed to capture only the advection of the scalar, thus minimising effects of diffusion (Ardakani et al., 2023).

Table 1
Discretisation lengths used to generate the volume mesh, with various levels of refinement in the different regions of the computational domain.

Computational region	Target surface size [mm]	Approximate number of cells (M)
Dome	2	7.3
Room	40	1.1
Left manifold	0.5	2.3
Right manifold	0.5	2.3
Left porous layer	1	1
Right porous layer	1	1

The model for the transport of aerosols assumes a one-way coupling, meaning that while the particle trajectories (or cloud of particles) are influenced by the flow field, the particles themselves do not impact the flow. Additionally, the aerosols are assumed to be dispersed, signifying that discrete particles are tracked independently through the surrounding fluid and do not exert any influence on each other. The numerical implementation of the particle tracking adopts a Lagrangian reference frame, hence one which moves with the particle. The force balance equation to determine the instantaneous position of the particle, and thus its trajectory, is given by

$$m_p \frac{d\boldsymbol{u}_p}{dt} = \sum \boldsymbol{F}_n \tag{15}$$

where m_p is the particle mass, $\boldsymbol{u}_p$ is the particle velocity and $\boldsymbol{F}_n$ represents the forces acting on the particle. In this work, we consider only the drag force, $\boldsymbol{F}_d$, the gravitational force, $\boldsymbol{F}_g$, and buoyancy force, $\boldsymbol{F}_b$. The drag force is given by

$$\boldsymbol{F}_d = \frac{1}{2} C_D \, \rho \, A \, |\boldsymbol{u} - \boldsymbol{u}_p| \, (\boldsymbol{u} - \boldsymbol{u}_p) \tag{16}$$

where C_D is the drag coefficient and A is the area of the particle projected on a plane perpendicular to the flow direction. Here we assume that particles are spherical and hence $A = 0.25\pi d_p^2$, where d_p is the particle diameter. The Schiller-Naumann correlation was employed for the drag force coefficient (Schiller, 1933), and is given by

$$C_D = \begin{cases} \frac{24}{Re_d}\left(1 + 0.15\ Re_d^{0.687}\right) & 0 < Re_d \leq 1000 \\ 0.44 & Re_d > 1000 \end{cases} \tag{17}$$

where $Re_d = \rho|\boldsymbol{u} - \boldsymbol{u}_p|d_p/\mu$ is the particle Reynolds number. The combined effect of gravitational and buoyancy forces is given by

$$\boldsymbol{F}_g + \boldsymbol{F}_b = (m_p - m_f)\boldsymbol{g} = m_p \left(1 - \frac{\rho}{\rho_p}\right) \boldsymbol{g} \tag{18}$$

where m_f is the fluid mass displaced by the particle, and $\rho_p = 916.72$ kg m^{-3} is the density of the particle (assumed to be water ice, hence similar though slightly less than water).

2.5. Numerical schemes, model setup and boundary conditions

The numerical simulations were carried out using STAR-CCM+ (15.06.007-r8 Siemens), a finite-volume solver. The flow and particle motion was modelled as unsteady and the time step was set to $\Delta t = 10^{-3}$ s. The implicit SIMPLE algorithm was employed to couple the pressure and velocity field in a segregated manner. The temporal and spatial schemes were set to second-order accuracy.

All particles were assumed to be of constant diameter of 10 μm, as this was identified as a representative aerosol size involved in transmission of infection. No size change was considered, hence change due to the condensation or evaporation effects, for example, have been neglected. Evaporation can occur in brief time periods and may affect the particle transport (Calmet et al., 2021; Liu et al., 2017), however due to the forced ventilation within the device these considerations may be seen as refinements to the present modelling.

The computational domain consists of five sub-regions joined by means of appropriate interfaces: two porous filters, two external manifolds, the dome, and the room space. The virtual model of the room, detailing the space in which the clinical setting experiments were carried out, was reproduced with particular care to replicate the main features: dimensions, location of the device, and appropriate boundary conditions, as shown in Figs. 1–3.

The volumetric mesh generated for the simulation consists of approximately 15 M polyhedral elements. Fig. 4 presents snapshots of the mesh element distribution across the domain. To achieve localised mesh refinement without compromising the overall optimised mesh size, the mesh was refined based on sub-region size and the underlying fluid dynamics. In particular, the size of the mesh elements was smallest within the manifolds and largest for the room space. The range of the volume mesh is reported in Table 1. A uniform mesh refinement was implemented within the dome volume, as this accommodates the varied flow dynamics exhibited, including the air curtains, flows from the mouth, nostrils, through the lateral openings and the suction hole. The choice of mesh size was based on the Taylor microscale to ensure that the turbulence modelling would be adequate. Mesh convergence investigation within the dome space was carried out with a target surface mesh size of 1 mm (hence below the Taylor microscale), resulting in 25 M cells.

Boundaries of the room that are artificial truncations of the domain were set to a zero *pressure* boundary condition ($p = 0$ Pa), while solid boundaries were set to a *no-slip* boundary condition ($\mathbf{u} = 0$ m s^{-1}). Forced ventilation or other forms of air movement

in the room was not considered. The walls of the device were set to *rebound* particles upon contact; while this does not replicate real-world scenarios, as it does not allow deposition to occur, this boundary condition serves as challenging numerical simulation test scenarios in that all aerosols are retained in suspension unless they are extracted via the suction hole or leave the domain.

The suction hole outflow and the external manifold inlets were both specified as *mass flow rate* boundary conditions. A hand-held anemometer was used to obtain an average flow rate at the manifold inlets and the suction hole when the device was disassembled in order to allow appropriate access. The average flow rates were found to be 9117 lit min^{-1} at the suction hole and 1539 lit min^{-1} at the manifold inlets. These values resulted in an average flow speed of 11.22 m s^{-1} at the suction hole, 9.74 m s^{-1} at the manifold inlets and 8 m s^{-1} at each air curtain jet.

To consider effects of exhalation, the mouth and nostril sections were also identified as inflow boundary conditions. Uniform velocity profiles were imposed, with a volume flow rate set to 600 lit min^{-1} for the mouth and 90 lit min^{-1} for each nostril (Calmet et al., 2019). The mouth flow rate is assumed as a worst case scenario, considering a typical male lung capacity is approximately 6000 ml, and assuming a sudden exhalation to occur in ∼0.6 s (note strenuous sniffing occurs on a similar time scale (Bates et al., 2015; Rennie et al., 2011)), resulting in a volume flow rate of 10 lit s^{-1} as an indicative value. The exhalation is hence an impulsively delivered violent event, with the aim of greatly affecting the airflow within the dome.

The Reynolds number at the sections where boundary conditions are imposed falls within the range $Re = [15239, 83780]$, where the minimum occurs at the nostrils and the maximum at the dome suction hole. Consequently one may expect turbulent flow and the $k - \omega$ SST model was employed for modelling turbulence, being a Reynolds Averaged Navier–Stokes (RANS) two-equation model (Menter, 1994).

The particles were released from a spherical surface with a radius of 4 cm and with the centre located at the centre of the mouth inlet tip. Different velocity magnitudes for spray droplets and dental debris have been reported in the literature (Juraeva, Park, Ryu, & Song, 2017; Nishi, Fushimi, Shimomura, & Hasegawa, 2018; Sergis et al., 2021). Considering a dental handpiece operating at 400,000 rpm with 1 mm burr radius, the linear velocity of the burr is 400 m s^{-1}. As a result, the injection velocity of particles was set to 400 m s^{-1}, which is among the highest values reported, in the direction normal to the injection surface at the injection point (Sergis et al., 2021). The particles were modelled as spherical solids, with a density similar to water and a diameter of 10 μm. The number of particles employed was ∼0.1 M and an independence investigation was carried out for Case 2 with ∼0.5 M particles.

2.6. Computational setup configurations investigated

In order to study the performance of the device in different scenarios, five test cases were considered. In practice, these investigated the relative effects of expiration and the importance of sealing the dome base (just below the patient's head) in a combinatorial fashion. Additionally, the protrusion of two cylinders into the dome space were considered, replicating the presence of the dental practitioner's arms in a representative configuration.

Case 1 dome base is **sealed**, **no flow** from mouth and nostrils;
Case 2 dome base is **sealed**, **flow** from mouth and nostrils;
Case 3 dome base is **open to the room**, **no flow** from mouth and nostrils;
Case 4 dome base is **open to the room**, **flow** from mouth and nostrils;
Case 5 dome base is **sealed**, **flow** from mouth and nostrils, **two cylinders are placed in the dome**.

In Cases 3 and 4 the base of the dome is set to be an interface condition, thus retaining the same mesh for the numerical simulations for Cases 1-4. Case 2 illustrates the envisaged standard use of the device under challenging conditions, with Case 5 representing a modestly more realistic scenario.

The patient's head is angled towards the left opening at 20 degrees from the vertical axis, following common practice during dental procedures. This setup results in a more challenging test case since the left opening will be more vulnerable to aerosol escape.

2.7. Experimental setup of clinical setting

An experimental study was conducted to assess the device's performance in a clinical setting, utilising an open-plan clinic bay. The trials were carried out on a dental simulation unit (DSU) featuring both upper and lower jaws. These experimental investigations aimed to replicate the real clinical practice and procedures faithfully. During the experiments, a clinical operator applied a human salivary amylase solution (100 U/ml) to the teeth of the DSU at a physiologic rate. The dispersal of salivary amylase aerosols was monitored by carefully placing 0.5% (w/v) starch agar plates at defined locations around the DSU (Devker et al., 2012).

Three AGPs were performed on the DSU jaws, with and without the dome-shaped device. These AGPs included: (i) examination of upper and lower anterior teeth utilising a 3-in-1 air and water spray for one minute; (ii) ultrasonic scaling of upper and lower anterior teeth for one minute; (iii) class IV cavity preparation using a high-speed handpiece on the upper right central incisor for one minute. The same AGPs were repeated by the same operator without the device. Throughout each AGP, a physiologically appropriate rate of salivary amylase application to the DSU jaw teeth was maintained using a Monoject syringe.

The evaluation of aerosol generation and dispersion involved the quantification of clearance zones on starch agar plates positioned at various distances from the working field. A total of 20 starch agar plates were strategically placed, including on the patient (DSU), dentist, dental nurse, and both inside and outside the device (the dome). The arrangement of the agar plates in the experimental setup is illustrated in Fig. 5. Following each procedure, the starch plates underwent incubation at 37 °C for 16 h.

Fig. 5. Location of agar plates in the clinic bay. The agar plates were placed at different locations, including on the shoulders and hands of the dentist and the nurse, as well as around the bay.

Subsequently, Lugol's iodine (1%, 10 ml) was applied to the surface of each plate for 1 min, followed by rinsing with distilled water and imaging using an Amersham Imager 680. A customised macro in Fiji/ImageJ was then employed to analyse each image and quantify the zone of clearance. The results of the image analysis are presented in Table 2, providing details on the location and label of the agar plates along with the detection of salivary amylase aerosol on each plate.

2.8. Experimental setup in laboratory

Experimental investigation of the device was also carried out in the laboratory setting, in which the effect of the single extraction as well as the air curtain were studied. A fog generator was used in 'burst mode' to emulate aerosol generation from AGPs within the oral cavity. Based on the fog generator and the diameter of the exhaust, the aerosol exit velocity from the oral cavity was estimated to be approximately $40 - 60$ m/s with an average burst operation of 1 s. With the extraction (i.e. suction hole) kept constant at a volume flow rate of 150 $m^3\ h^{-1}$, variations in the setup were investigated, including: (i) sealing the base of the dome or leaving it open to the room; (ii) varying the volume flow rate of the air curtains covering the lateral access openings, from no jet to a maximum jet flow rate of approximately 16 $m^3\ h^{-1}$; (iii) retaining solely the lower array of jets active. It is useful to mention that the volume flow rates are measured by a Testo 405i hot-wire anemometer with an uncertainty of 5% across the range of velocity measured. Moreover, the measurements were taken at the inlet of the suction hole and the outlet of the air curtains, respectively, hence the pressure drops through the pipe systems have already been accounted for. To ensure consistency of the observation, 10 runs were performed for each operating scenario investigated, and the test set-up is shown in Fig. 6. Subsequently, the representative cases were presented below for the qualitative assessment of the device design.

3. Results

Experimental and computational investigation into the effectiveness and working dynamics of the device were carried out. The experimental work in the clinical bays was carried out by clinical operators with the aim of closely replicating real practice. The experimental work in the laboratory made use of hand-held anemometer measurements and visual recordings. The computational investigation made use of high-resolution spatial and temporal data obtained from the numerical simulations, enabling a more in-depth investigation.

3.1. Results from experiments in clinical bays and laboratory settings

The experimental results carried out in a clinical bay report the presence or absence of salivary amylase on agar plates positioned at numerous strategic locations. Three different AGPs were investigated, as commonly carried out in standard practice. The results are detailed in Table 2, from which the key result is that the use of the device markedly reduces the spread of aerosols outside the dome. Indeed, across the three sets of experiments involving AGPs, a clear and clinically significant reduction in amylase clearance was observed when using the device. This indicates that the device is overall effective in containing the aerosols generated to within the dome. Nevertheless, some amylase was detected on agar plates external to the dome and further investigation is required, though preliminary findings indicate that the build of the device prototype allowed some leakage which we do not expect in a follow-up build.

The results of experiments carried out in the laboratory can be considered visually in Fig. 6. From these results, we observe that the aerosols are successfully directed towards the extraction hole, which proves to be effective and of primary importance in their

Table 2
Results from the clinical bay test of the protective device conducted by a clinical operator on a Dental Simulation Unit (DSU). In this table, 'Y' and 'N' represent evidence of amylase clearance and no evidence of amylase clearance, respectively. In Experiment D, one of the plates was spoilt and is shown by the dash line.

Position of agar plate	Without device						With device					
	Experiment A (20 plates) 3 in 1		Experiment B (20 plates) High speed		Experiment C (20 plates) Ultrasonic		Experiment D (20 plates) 3 in 1		Experiment E (20 plates) High speed		Experiment F (20 plates) Ultrasonic	
	Plate	Result	Plate	Result	Plate	Result	Plate	Result	Plate	Result	Plate	Result
Operator right shoulder	A_1	Y	B_1	Y	C_1	Y	D_1	N	E_1	N	F_1	N
Operator mask	A_2	Y	B_2	Y	C_2	N	D_2	N	E_2	N	F_2	N
Operator left shoulder	A_3	Y	B_3	Y	C_3	N	D_3	N	E_3	N	F_3	N
Nurse right shoulder	A_4	Y	B_4	Y	C_4	N	D_4	N	E_4	N	F_4	N
Nurse mask	A_5	Y	B_5	N	C_5	N	D_5	N	E_5	N	F_5	N
Nurse left shoulder	A_6	Y	B_6	N	C_6	N	D_6	N	E_6	N	F_6	N
30 cm right of operator	A_7	Y	B_7	N	C_7	N	D_7	N	E_7	N	F_7	Y
60 cm right of operator	A_8	N	B_8	N	C_8	N	D_8	N	E_8	N	F_8	N
100 cm right of operator	A_9	N	B_9	N	C_9	N	D_9	N	E_9	N	F_9	N
30 cm right of nurse	A_{10}	Y	B_{10}	N	C_{10}	N	D_{10}	N	E_{10}	N	F_{10}	N
60 cm right of nurse	A_{11}	N	B_{11}	N	C_{11}	N	D_{11}	Y	E_{11}	N	F_{11}	N
100 cm right of nurse	A_{12}	N	B_{12}	N	C_{12}	N	D_{12}	N	E_{12}	N	F_{12}	N
Operator right hand	A_{13}	Y	B_{13}	Y	C_{13}	Y	D_{13}	–	E_{13}	N	F_{13}	N
Operator left hand	A_{14}	Y	B_{14}	Y	C_{14}	N	D_{14}	N	E_{14}	Y	F_{14}	N
Nurse right hand	A_{15}	Y	B_{15}	Y	C_{15}	N	D_{15}	N	E_{15}	N	F_{15}	N
Nurse left hand	A_{16}	Y	B_{16}	Y	C_{16}	Y	D_{16}	Y	E_{16}	N	F_{16}	N
Patient forehead	A_{17}	Y	B_{17}	Y	C_{17}	N	D_{17}	Y	E_{17}	Y	F_{17}	Y
Patient shoulder right	A_{18}	Y	B_{18}	Y	C_{18}	N	D_{18}	Y	E_{18}	Y	F_{18}	Y
Patient shoulder left	A_{19}	Y	B_{19}	Y	C_{19}	Y	D_{19}	Y	E_{19}	Y	F_{19}	Y
Overhead chair light	A_{20}	N	B_{20}	N	C_{20}	N	D_{20}	N	E_{20}	N	F_{20}	N

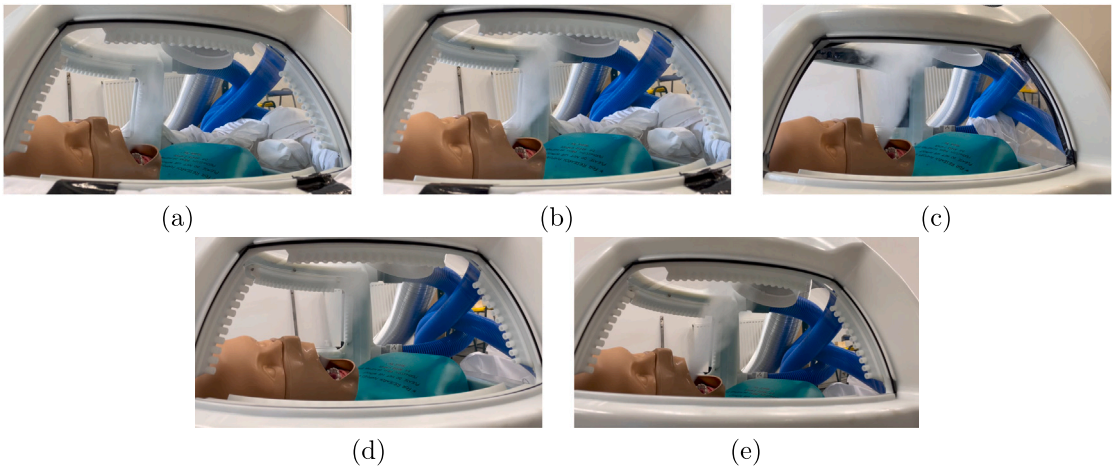

Fig. 6. Smoke visualisation of some of the experiments carried out in the laboratory. (a) Dome base is closed, air curtain is on. (b) Dome base is closed, air curtain is off. (c) Dome base is open, air curtain is formed from solely the bottom row of jets along the access side openings. (d) Dome base is open, air curtain is on. (e) Dome base is open, air curtain is off.

removal. It was also noted that sealing the dome base is needed for the device to work effectively with the air jets over the access side openings, essentially creating a inward favourable pressure gradient. The effectiveness of additional air curtains surrounding the access panel was investigated, and this sensitivity study suggests a secondary importance in the efficacy of the device, with some acceptable tolerance.

Variations of the prototype design investigated included employing solely the lower array of jets around the side access openings to form the air curtains. This configuration performed favourably and reduced the complexity of flow structures within the dome. However, further investigation is needed to optimise the air jet layout, with considerations also of the device in use, hence with the practitioner's arms inserted through the side openings. Flexible flaps across the openings were also briefly investigated, and while clearance performance improved visually, the practicality of these in a clinical setting would need to be evaluated.

A survey of the velocity field around the manikin's face during maximum suction and air curtain flow rates reveals that the velocity remains below 1.2 m s^{-1}.

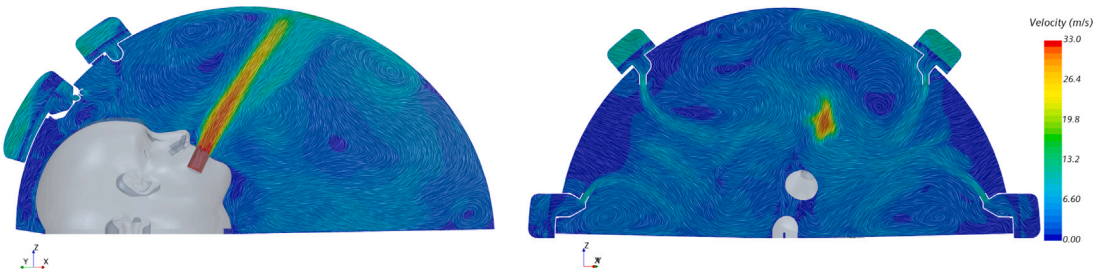

Fig. 7. Results from Case 2, showing detail of velocity magnitude [m s^{-1}] and its line integral convolution in cross-sections A (left) and B (right), shown in Fig. 3(a).

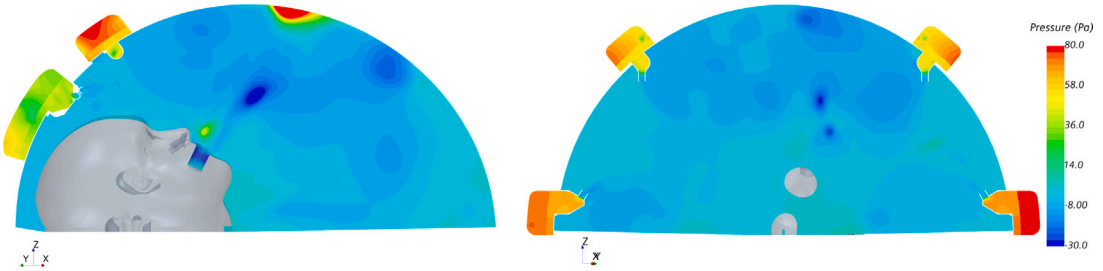

Fig. 8. Results from Case 2, showing detail of pressure [Pa] in cross-sections A (left) and B (right).

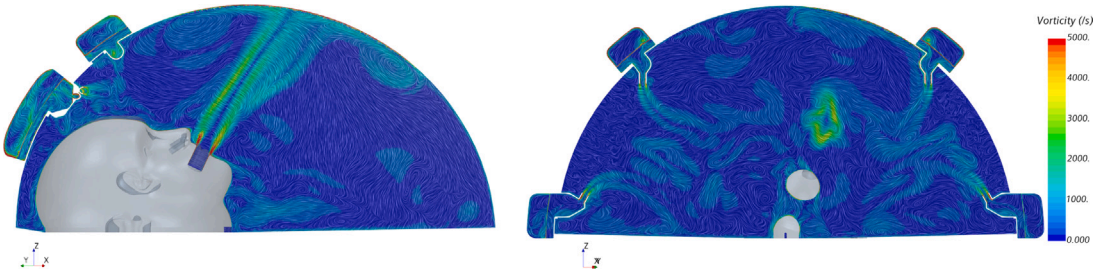

Fig. 9. Results from Case 2, showing detail of vorticity magnitude [s^{-1}] and its line integral convolution in cross-sections A (left) and B (right).

3.2. Results from numerical simulations

Numerical simulations were run for 12 s without aerosols, allowing for the flow to reasonably develop within the dome and avoid marked transient effects associated with the choice of initial conditions. Having attained the quasi-developed flow, at 12 s, the particles were released into the domain and the numerical simulations continued for a further 2 s to 4 s until the particles were removed from the dome either by escape through the side openings or extraction by the pump. Results presented here are related to the time after the aerosols were introduced into the domain, hence $t > 12$ s.

3.2.1. Flow field

To relate the flow dynamics inside the dome space, the flow characteristics on cross-sections A and B (shown in Fig. 4a) are investigated. For Case 2 at $t = 12$ s, the flow velocity magnitude and its line integral convolution are presented in Fig. 7. It is apparent that the jet flow from the mouth impacts the dome, generating a high-pressure region as identified in Fig. 8. As the expiration jet impinged on the dome wall, a thin radially advancing flow along the wall is observed, sustaining an annular vortex roll-up at its leading edge which bulges into the dome space. Experimental and computational investigations of turbulent jets impinging on flat surfaces have also reported similar dynamics (Hassan et al., 2013; Liu et al., 2010). The strength of these vortices may be inferred by the low pressure regions at the vortex core, effecting a centripetal force, though they are more readily identifiable from the vorticity magnitude, as shown in Fig. 9. In this figure, we also observe that high vorticity magnitude is present in the shear layer formed around the expired jet and the air curtain jets.

Regions of high pressure are identified in the manifold upstream of the porous layer (see Fig. 8), which results in a near-uniform velocity from the lateral jets, as reported in Fig. 7. This suggests the inclusion of the porous layer within the manifold is effective,

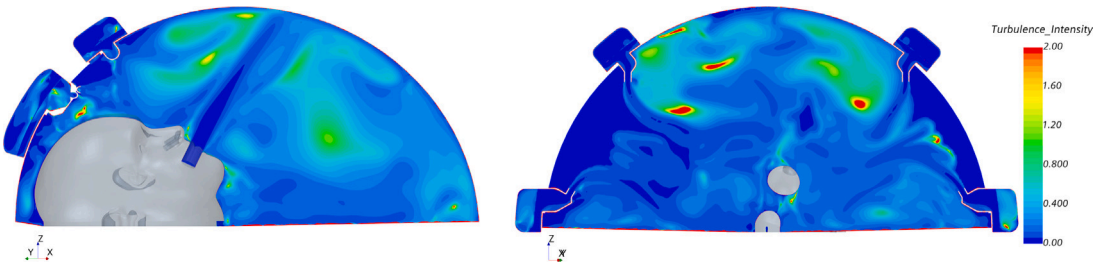

Fig. 10. Results from Case 2, showing detail of turbulence intensity in cross-sections A (left) and B (right).

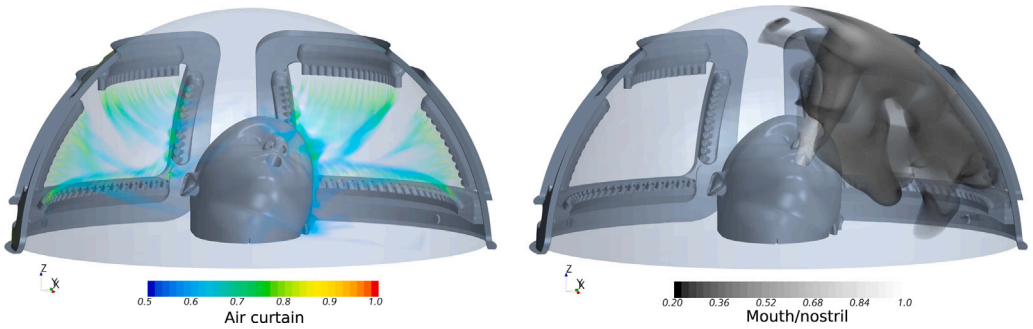

Fig. 11. Results from Case 2, showing three-dimensional rendering visualisation of passive scalars from the air curtain (left) and mouth/nostril flows (right).

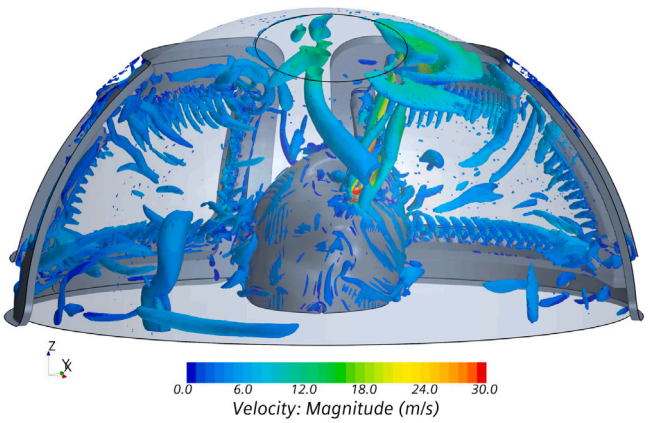

Fig. 12. Results from Case 2, showing vortex structures in the dome visualised by Q-criterion iso-surface at $Q = 40000\ s^{-2}$, coloured by velocity magnitude [m s^{-1}].

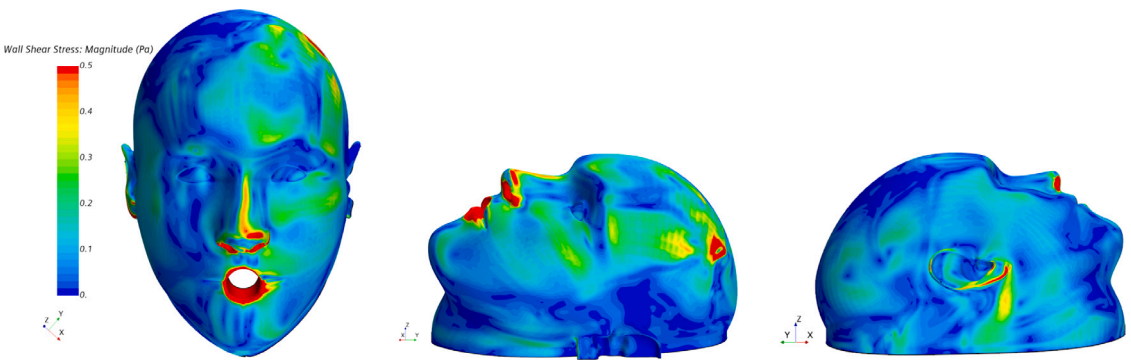

Fig. 13. Results from Case 2, showing wall shear stress magnitude [Pa] distribution on the patient's face.

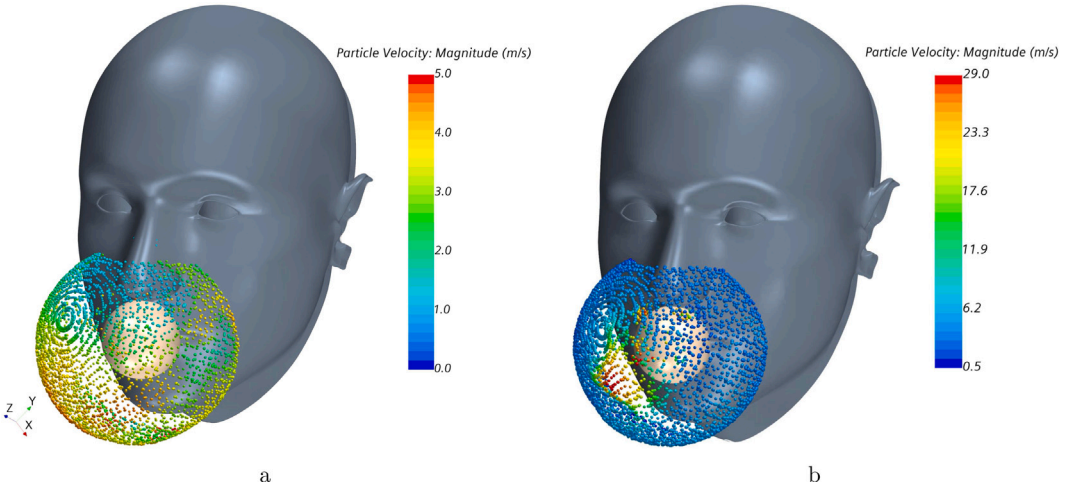

Fig. 14. The injection surface (white sphere) and particle locations after one time step from release, $\Delta t = 0.001$ s. (a) Mouth/nostril flow is turned off (Case 1); (b) Mouth/nostril flow is turned on (Case 2). The injection velocity of particles is 400 m s^{-1}.

Table 3
Outcome of particle trajectories, detailing the relative fraction of particles by boundary through which they left the dome space.

	Num. injected particles ($\times 10^3$)	Extraction (%)	Left opening (%)	Right opening (%)	Dome base (%)
Case 1	106	100	–	–	–
Case 2	106	>99.99	<0.1	–	–
Case 3	106	>96	–	<0.003	<3
Case 4	106	<97.4	<0.41	<0.016	<2
Case 5	106	>99.93	<0.07	–	–

evenly distributing the flow rates of the jets. The air curtain is formed through the series of jets that together creates a layer of comparatively high-momentum flow near the lateral openings.

Fig. 10 presents the turbulent intensity on the cross-sections A and B. The regions of high intensity correlate with the presence of rapid flow deceleration, such as in the vortex roll-up along the dome wall. Additionally, within the dome space, multiple regions of higher turbulent intensity can be readily observed, underscoring a complex flow field caused by the multiple sources of airflow, including air curtains, expiration and extraction. Of particular interest, we note that the area behind the air curtain and closer to the lateral openings exhibits low turbulent intensity, and is separated from the more energetic internal flow by the air curtain.

A palpable visualisation of the air curtain geometry is provided in Fig. 11a, given as the volumetric render of a passive scalar concentration emanating from the jets. The range is chosen such that the flow patterns of the more persistent features can be readily observed. The jets combine and appear as pyramidoidal surfaces that effectively form the air curtains across the dome openings. To visualise the efficacy of the air curtains in a similar fashion, in Fig. 11b, the volumetric render of a passive scalar concentration emanating as expired air is provided. From this figure, we readily observe that no scalar is seen external to the dome space, despite the patient's head being angled towards the left lateral opening.

In Fig. 12, Q-criterion iso-surface at $Q = 40000$ s^{-2} identifies coherent structures around air jets in the dome, in that enstrophy density dominates over strain production. Concentrated at jet initiation points, the iso-surfaces gradually diminish away from the origin, suggesting elevated vorticity at initial stages of jet formation, which then dissipates as the jets reach further into the dome.

Fig. 13 displays the contour of wall shear stress on the manikin's face, as an indicator of patient comfort. The left side of the face exhibits higher skin friction compared to the right side. The tilting of the head to the right positions the left side of the face closer to the air curtain, resulting in the observed asymmetry in WSS. The boundary layer formed by the bulk flow is crucial in near-wall heat transfer and human thermoregulation (Gan, 1994; Martinho, Lopes, & da Silva, 2012; Tanabe, Kobayashi, Nakano, Ozeki, & Konishi, 2002). The multi-factored attributes that affect a perceived *thermal comfort* of an individual has been extensively studied (Fanger, 1970) and can be readily rated (Tartarini, Schiavon, Cheung, & Hoyt, 2020). These works suggest that a temperature of ~25 °C, but otherwise standard ambient conditions, would ensure thermal comfort for the patient. However, since it is only the patient's head that is exposed to the airflow and not the entire body, we may expect modest differences to the thermal comfort correlations reported in the literature, and further investigation is required.

3.2.2. Particle dynamics

The particle dynamics and transport in the dome is dependent on the flow field and will have direct implications on possible pathogen transmission. The particles were released at $t = 12$ s and the simulation was run until the fate of all the particles in the

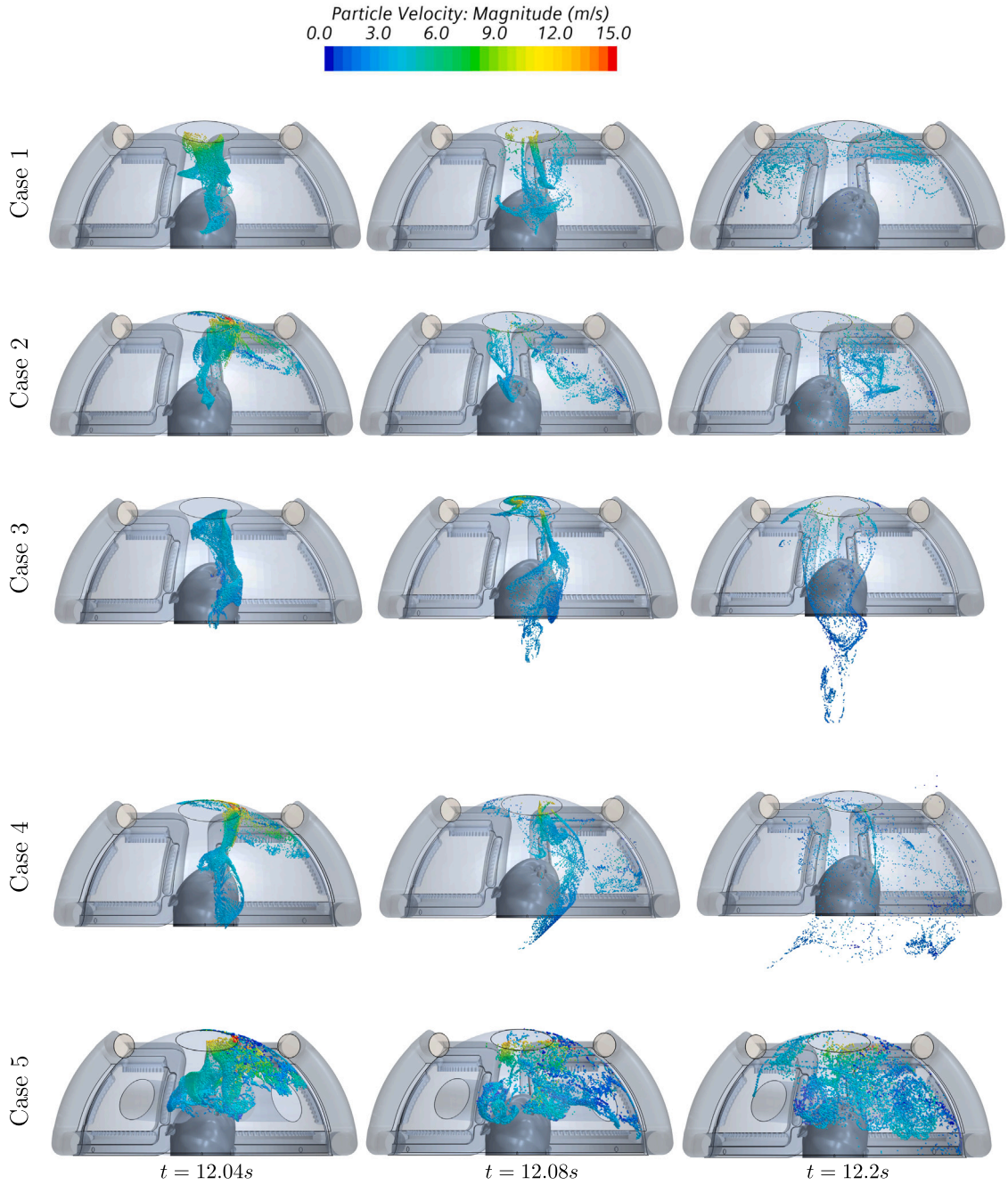

Fig. 15. Solution of particle transport in dome for three time instances coloured by particle velocity magnitude.

dome was determined. Particles were injected at four time intervals of $\Delta t = 0.001$ s from the hemispherical surface located in front of the mouth, as illustrated in Fig. 14, ensuring that particles are released in all directions into the dome. The total number of simulated particles is approximately 106×10^3 (see Table 3).

Particle locations at $\Delta t = 0.001$ s after the release time are shown in Fig. 14 for Cases 1 and 2, which are with and without expiration, respectively. The initial particle velocities are set uniformly to 400 m s^{-1} normal to the injection surface, however their speed rapidly decreases owing to the drag on the aerosols. Indeed, at $\Delta t = 0.001$ s after the release time, the particle speeds on the whole reach no more than 5 m s^{-1} unless they lie in front of the high momentum oral flow.

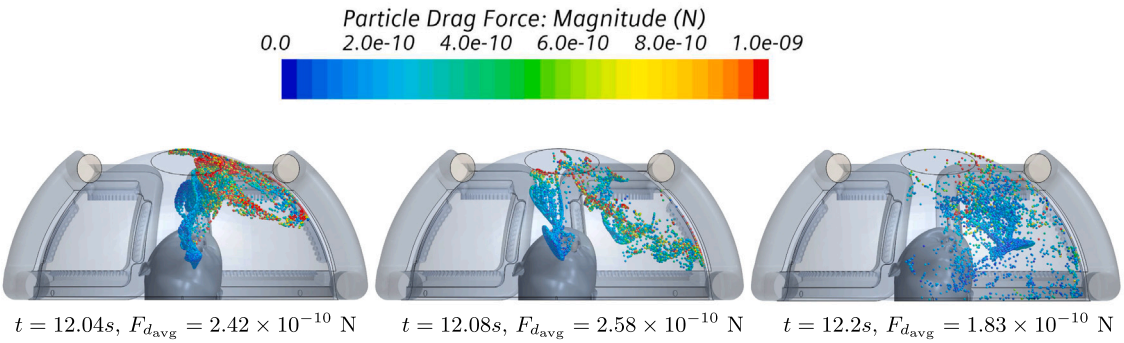

Fig. 16. Particle drag force for Case 2 at three time instances. The average drag force is reported, while the magnitude of the gravity force is 4.7×10^{-12} N, which suggests it exerts minimal influence on particle transport within the dome.

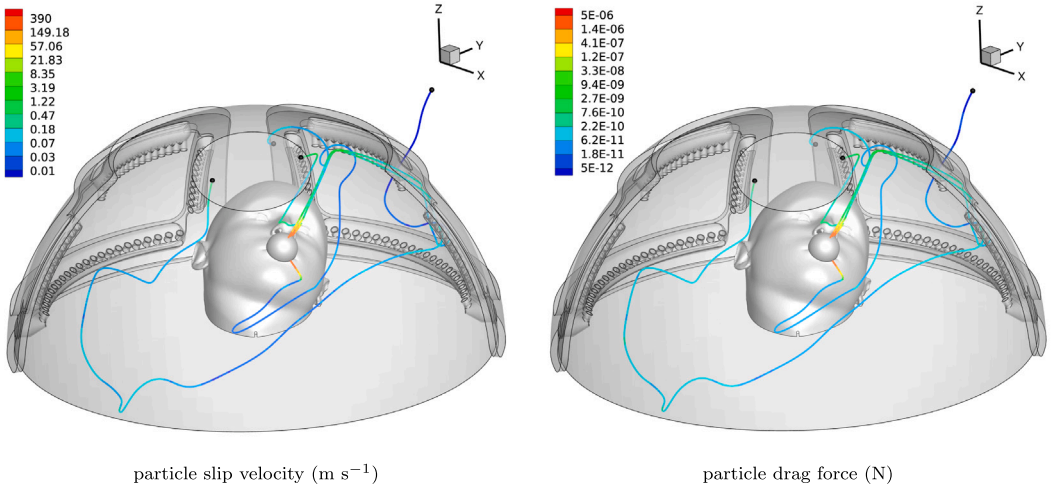

Fig. 17. Results from Case 2, showing trajectories of four particles released from different positions on the injection surface.

Fig. 15 shows the particle position in the dome at three time instances: t = 12.04 s, t = 12.08 s, and t = 12.2 s. These time instances were chosen for visual convenience, such that the effect of suction hole, air curtain and bulk flow on particle transport in the dome can be observed during the early stages of particle release.

It is evident from Table 3, which reports the number of particles crossing each boundary of the dome, that for all cases investigated, the majority of particles are extracted via the suction hole. This occurs even though the head is angled to the left. Notably, in Cases 1 and 2, where the base of the dome is sealed, the device exhibits excellent performance in confining and extracting the airborne micro-particles. Indeed, in Case 1, no particles escaped into the room, while in Case 2, a minor number (<0.1%) find their way to the room space through the left opening. Conversely, in Cases 3 and 4, a greater number (<3%) of particles exits from the base of the dome, emphasising the crucial role of sealing the dome space from below in minimising particle dispersion external to the dome.

The suction hole plays a crucial role in the particle dynamics within the dome. It is observed from Fig. 15 that on the whole, particles progressed towards the suction hole during the early stages after injection, and indeed a well-defined particle plume is observed in all cases at t = 12.04 s (hence Δt = 0.04 s after aerosol ejection). These dynamics are driven by the high relative flow rate of the suction hole. When flow from the mouth/nostril is present, the particles also experience the expired funnel-shaped high velocity jet, as illustrated in Figs. 11 and 14, which greatly affects the trajectories of the aerosols promptly after their injection.

The high momentum expired flow is not seen to significantly affect this extraction, as evidenced by comparing Case 1 with 2 and Case 3 with 4. As the expired flow impinges on the dome, some particles are transported by the rolling vortices along the dome inner wall and subsequently disperse throughout the dome, transported by the complex internal flow dynamics. For these particles, the air curtains maintain a high momentum flow barrier to prevent escape through the side opening in the dome, but additionally there is low momentum air ingress from these openings, which maintains a constant flow into the dome. The majority of these dispersed particles are redirected to the central zone of the dome and out through the suction hole, albeit with different elapsed times.

As reported in Table 3, a small number of particles exited the dome through the side openings for some Cases tested. While the quantity of escaped particles is negligible relative to the total number of injected particles, and this prototype device is seen to be effective in drastically reducing contamination and as such improving the safeguarding of the medical practitioners, it is nevertheless important to identify the mechanisms that led the particles to escape the dome space. To this end, the dominant forces experienced by the particles are shown in Fig. 16 for three distinct time instances. Following injection, particles undergo high drag due to the elevated slip velocity resulting in a rapid deceleration, and subsequently particles are entrained in the expired air jet and flow dynamics within the dome. The drag force notably increases in radial proximity to the suction hole, since it acts as a sink, as well as along the dome wall where higher velocity gradients and vorticity production occur. From Fig. 16 it is noticeable that the drag force on the whole is the dominating effect the aerosol experiences, surpassing the force due to gravity.

Four particle trajectories are plotted in Fig. 17, showing instances when particles leave the dome through the left side opening as well as correctly via the suction hole. The particles are released at the same time from different locations on the injection surface. It is evident that the paths traced out by each particle are diverse, underscoring the complexity of the flow structures within the dome space. The large drag force along the initial portion of the trace indicates a rapid deceleration after aerosolization, though subsequently a rather constant drag force magnitude is observed for the remainder of the traces. Again, we observe a higher drag force in radial proximity to the suction hole as well as long the dome wall in proximity to the location of expired jet impingement. The slip velocity closely follows the drag force along the traces. On close inspection, we can identify the corners of the access side openings as the locations where the escaped particles exit the dome. In these locations, there is a space in the air curtain in this prototype device, as the air jets are presently placed along each of the edges of the side openings but not continuously along the perimeter.

In the simulation results for Case 5, in which the protrusion of cylinder-like geometries mimics the dental practitioner's arms, the airflow is greatly disrupted during the early times after particle injection, such that the particle plume is rapidly dispersed within the dome space. It is therefore of particular interest that we observe from Table 3 that the particles escaping the lateral openings are of the same order as for Case 2. This suggests that the insertion of arms to treat the patient does not incur an additional risk of particle escape and spread in the room space. The air curtain provides a layer of high momentum airflow that flows along and around external objects inserted into the dome. Furthermore, the presence of the arm causes blockage in the lateral opening cross-sectional area, causing the ingress of air through the lateral opening to have higher momentum and effect greater protection from particles escaping.

4. Discussion

The prototype device developed and tested is intended for use by dental practitioners during routine procedures, but in particular those in which aerosols are actively generated. The device consists of four principal mechanisms to eliminate or reduce aerosol spread: (i) a rigid barrier to delimit the contaminated air and capture any large and high momentum particles; (ii) an air curtain as a high momentum airflow layer, which is effective in sealing access side openings and redirecting the flow towards the centre of the dome; (iii) a low momentum airflow ingress at the access side openings to ensure that a constant stream towards the suction hole is maintained; (iv) a suction hole located in the device to extract the contaminated air. The action of each of these mechanisms on the fluid dynamics and the particle transport can be identified from the computational results. The efficacy of the compounded mechanisms is reported by the computational and experimental results.

The effectiveness of the dome-shaped device is realised by the flow characteristics dictated by its design. Multiple factors within the dome, such as mouth/nostril expired flow, air jets and the suction hole, exert a profound influence on the internal flow structures. The device is seen to perform well from both the computational and experimental investigations, successfully extracting most of the aerosols, and appears to be insensitive to some of the variations in the setup even though the internal flow structures are seen to change noticeably. Vigorously exhaled air flow, for example, can alter the velocity and trajectory of particles, though the device performance in extracting the particles through the intended suction hole is seen to be largely unchanged. Similarly, disruption to the flow within the dome, as is caused, for example, by inserting arms through the access side openings to carry out procedures on the patient, minimally increases the risk of particles escaping through side openings. The three key factors affecting the efficacy of the device are related to the volume flow rate of the extraction, the air curtains and the option of closing the base of the dome.

The air jets lining the perimeter of the access openings establish a protective barrier, in the form of an air curtain, comprising a high-momentum air stream across the openings. The primary role of the air curtains is to redirect the path of airborne particles, effectively impeding their motion through the side opening. Once contained within the dome, these particles can be extracted via the suction hole. The air curtains are seen to be particularly effective for Case 5, where mock medical practitioner's arms are inserted in the dome space to access the patient. The air jets are purposefully angled to envelop the inserted arms of the practitioner. The results for Case 5 show that the air curtains remain stable and attached to the cylinders introduced through the side openings. No significant difference in successful extraction between Case 5 and Case 2 is observed in Table 3, indicating an effective overall performance of the protective device during dental procedures.

Analysis of particle statistics at different boundaries, as reported in Table 2, demonstrates that closing the base of the dome is the most effective configuration for containment. The spherical shape of the dome directs high-velocity particles that escape from the adverse pressure gradient caused by the suction hole towards the base of the dome This potentially heightens the risk of particle spread if the base of the dome is not sealed. Interestingly, in Case 3, with no expired flow, more particles exited the dome from the base compared to Case 4, where a strong jet from the mouth/nostrils was present. This observation suggests that in Case 4, the

exhaled flow pushes particles towards the suction hole, enhancing their extraction, while in Case 3, those particles initially ejected randomly and towards the lower regions of the dome will then be falling due to gravity rather than be swept up by the flow.

Increasing the suction flow rate enhances particle extraction efficiency, and is the key mechanism in the successful functioning of the device, effectively acting as a point sink that gathers the flow. Overly large suction flow rates will, however, result in a decrease in pressure within the dome, potentially affecting the efficacy of the suction pump and may cause discomfort for patients, including from the noise generated in practice. The air jets effectively support the suction, acting to redirect and propel the flow towards the suction hole. This also counteracts the possibly adverse effect of lower pressure in the dome, thereby maintaining the pressure closer to atmospheric levels. Maintaining a balance between patient comfort and extraction flow rate will be an essential factor in optimising the functionality of the system.

While the suction flow rate is of primary importance, the dome remains an essential feature of the device, in that it provides containment of the space containing aerosols and importantly, it acts as a rigid barrier for those larger aerosols that may be formed during aerosol generating procedures. Alternative aerosol extraction devices, for example as proposed for surgical tracheotomy (Calmet et al., 2022), perform well in the case when the generated aerosols will be contained in a directed jet. However, in dentistry the aerosols may be ejected in any direction, and the dome provides the necessary mechanism to arrest and contain any high momentum aerosols. For example, from Eq. (6) the arrest distance for a 50 μm aerosol (with otherwise the same conditions as adopted in Section 2.2) is over 1 m, placing such aerosols within the surgery space where practitioners will traverse. The dome additionally serves to focus the sink effect of the suction hole, ensuring it is more effective.

From both the computed solutions and the experimental validation, a small number of aerosols did leave the dome space and were not successfully captured by the extraction system in this prototype design. From the numerical simulations, the cause of this was identified to be some gaps in the air curtain, namely at the corners of the access side openings where no jets are present, which can be readily amended. Additionally, it is important to ensure the base of the dome is sealed to avoid aerosols that are ejected in a direction of low elevation to escape through the bottom of the device. The alternative to closing the base would be to considerably increase the suction flow rate to ensure a sufficiently fast vertical flow is set up through the base to redirect these aerosols.

5. Conclusions

A protective device to confine airborne particles during dentistry procedures was developed and tested through laboratory experiments, in mock clinical settings and by means of numerical simulations. The device was designed in conjunction with dentistry practitioners by means of a survey during hands-on evaluation. It benefits a modular design, enhancing its portability, ease of assembly and cleaning. Its dimensions and wide access side openings comfortably accommodate the patient's head, medical staff's arms and tools, allowing for good manoeuvrability during medical procedures within the dome. From our extensive investigation, the reported volume flow rate proved effective in containing particles, even under extreme conditions.

It is essential, however, to acknowledge the limitations of our study. The numerical simulations utilised fixed parameters, such as particle diameter and ejection velocity, which are a subset of the more variable emission from AGPs. Additionally, active dentistry procedures were not modelled, but rather solely a mock setup of practitioner's arms introduced in the dome volume. The numerical results are supplemented by experimental data, which in contrast involved the release of droplet particles covering a broad range of particle diameters, both in a laboratory and in mock clinical settings. For these, however, a manikin model was used, thus resulting in a simplified setup without respiration.

A detailed computational fluid dynamics model was developed to investigate the mechanics of the airflow field within the device, as well as the dynamics of airborne particles generated during aerosol-generating procedures (AGPs). The number of particles passing different boundaries was monitored and reported in order to quantitatively assess the performance of the dome. Additionally, a passive scalar with a high Schmidt number was utilised to track the flow path within the dome. To complement the computational results, a thorough experimental investigation was conducted in an open clinic setting, with a dentist as the clinical operator, performing three dental AGPs on a dental simulation unit. Aerosol generation and spread were measured by quantifying clearance zones on 20 starch agar plates at different locations in the working area. Finally, laboratory experimentation was carried out with a hand-held anemometer and visual recordings to inspect the flow dynamics and test some setup variations.

The combined results of simulations and experiments highlight the dome's capability to contain and extract particles with high initial velocity. Optimal performance of the dome was observed when the base of the dome was sealed, preventing particles from exiting the dome via this boundary and allowing the suction hole to effectively eliminate particles from the interior space. While the dome provides access to medical practitioners via the side openings, the air jets were shown to be effective in enveloping external objects passing through the side opening, thereby effectively providing an air curtain to cover the openings.

Overall, the results presented in this work demonstrate the success of the device, presenting its potential in reducing airborne particle spread during operations where a close interaction with a patient's respiratory system is inevitable. The workings and the principal mechanisms of the device have been critically analysed and discussed. Recommendations have been provided with regards to what the key parameters are and how to improve the design.

CRediT authorship contribution statement

Vahid Goodarzi Ardakani: Writing – original draft, Visualization, Software, Methodology, Investigation, Formal analysis, Data curation. **Mojtaba Dorri:** Writing – review & editing, Project administration, Funding acquisition, Conceptualization. **Bin Zang:** Writing – review & editing, Visualization, Investigation. **Angela H. Nobbs:** Writing – review & editing, Investigation. **Stephen Cross:** Investigation. **Alberto M. Gambaruto:** Writing – review & editing, Writing – original draft, Supervision, Project administration, Methodology, Investigation, Formal analysis, Conceptualization.

Declaration of competing interest

The authors declare the following financial interests/personal relationships which may be considered as potential competing interests: Mojtaba Dorri reports financial support was provided by Bristol and Weston Hospitals Charity. Mojtaba Dorri reports financial support was provided by Elizabeth Blackwell Institute, MRC Confidence in Concept (CiC). Alberto Gambaruto has patent issued to University of Bristol. Mojtaba Dorri has patent issued to University of Bristol. If there are other authors, they declare that they have no known competing financial interests or personal relationships that could have appeared to influence the work reported in this paper.

Acknowledgements

The authors would like to thank Dr. Jane Brittan at Bristol Dental School for her technical assistance, Dr. Xiao Liu at the Faculty of Engineering for her assistance in laboratory tests, Duncan Casey for his contribution in design and developing commercialisation strategy, and Radhika Desai for helping with Patient and Public involvement and clinical tests. Vahid Goodarzi Ardakani gratefully acknowledges support from the University of Bristol to carry out his PhD studies. The work was supported by : (i) Bristol and Weston Hospitals Charity, grants Ref. A&B 2020-Spr-02: Patients' and clinician's expectations of and views on a NOVel patIent shield (NOVID); (ii) Elizabeth Blackwell Institute, MRC Confidence in Concept (CiC): Project Title: NOVel patlent shielD (NOVID) fEC number: 286862.

Appendix. Advisory group questions

An Advisory Group of healthcare professionals was tasked with providing feedback and insight, in order to inform the design of the device and its demand. The Advisory Group were provided some conceptual designs, a physical prototype and the following questions:

- What has the impact of COVID-19 been on your clinical practice?
- What are the main barriers for practicing routine dentistry during the pandemic?
- How do you feel about performing dental procedures under a clear dome like this (showing image)?
- Do you think whether patients would accept to be treated under a clear dome like this?
- The dome is likely to limit your access to the treatment area but will prevent the spread of the virus. If you had a choice, would you rather have:
  - 100% protection against the virus but limited access to the treatment area
  - Better treatment area access but accept the reduced risk of virus contraction i.e. not 100% protection
  - Others
- Please indicate where you prefer the access holes to be fitted?
- Would you prefer the dome to be attached to the dental chair or as a separate portable unit?
- Would you use this dome for AGPs or non-AGPs, or both?
- What evidence do you need to see before using a similar medical device?
- How much would you be prepared to pay for this medical device?

Data availability

The data that has been used is confidential.

References

Ardakani, V. G., Gambaruto, A. M., Grahamslaw, N., Garsed-Brand, G., Ault, R., Vaquero, E., et al. (2023). Heritage conservation with a surface air curtain: Use of CFD and sensor data with a near-wall region flow analysis. *Building and Environment*, Article 110640.

Bates, A. J., Doorly, D. J., Cetto, R., Calmet, H., Gambaruto, A. M., Tolley, N., et al. (2015). Dynamics of airflow in a short inhalation. *Journal of the Royal Society Interface*, *12*(102), Article 20140880.

Calmet, H., Bertomeu, P. F., McIntyre, C., Rennie, C., Gouder, K., Houzeaux, G., et al. (2022). Computational modelling of an aerosol extraction device for use in COVID-19 surgical tracheotomy. *Journal of Aerosol Science*, *159*, Article 105848.

Calmet, H., Inthavong, K., Both, A., Surapaneni, A., Mira, D., Egukitza, B., et al. (2021). Large eddy simulation of cough jet dynamics, droplet transport, and inhalability over a ten minute exposure. *Physics of Fluids*, *33*(12).

Calmet, H., Yamamoto, T., Eguzkitza, B., Lehmkuhl, O., Olivares, E., Kobayashi, Y., et al. (2019). Numerical evaluation of aerosol exhalation through nose treatment. *Journal of Aerosol Science*, *128*, 1–13.

CD-adapco (2017). *STAR-CCM+ user guide version 12.04*. New York, NY, USA: CD-Adapco.

Devker, N. R., Mohitey, J., Vibhute, A., Chouhan, V. S., Chavan, P., Malagi, S., et al. (2012). A study to evaluate and compare the efficacy of preprocedural mouthrinsing and high volume evacuator attachment alone and in combination in reducing the amount of viable aerosols produced during ultrasonic scaling procedure. *The Journal of Contemporary Dental Practice*, *13*(5), 681–689.

Doorly, D., Taylor, D., & Schroter, R. (2008). Mechanics of airflow in the human nasal airways. *Respiratory Physiology & Neurobiology*, *163*(1–3), 100–110.

Ehtezazi, T., Evans, D. G., Jenkinson, I. D., Evans, P. A., Vadgama, V. J., Vadgama, J., et al. (2021). SARS-CoV-2: characterisation and mitigation of risks associated with aerosol generating procedures in dental practices. *British Dental Journal*, 1–7.

El Hassan, M., Assoum, H., Martinuzzi, R., Sobolik, V., Abed-Meraim, K., & Sakout, A. (2013). Experimental investigation of the wall shear stress in a circular impinging jet. *Physics of Fluids*, *25*(7).

Fanger, P. O. (1970). *Thermal comfort. Analysis and applications in environmental engineering*. New York: McGraw-Hill.
Feng, Y., Marchal, T., Sperry, T., & Yi, H. (2020). Influence of wind and relative humidity on the social distancing effectiveness to prevent COVID-19 airborne transmission: A numerical study. *Journal of Aerosol Science*, *147*, Article 105585.
Gan, G. (1994). Numerical method for a full assessment of indoor thermal comfort. *Indoor Air*, *4*(3), 154–168.
Goodarzi Ardakani, V. (2023). *Transport of suspended particles in physiological flows with a focus on the near-wall flow field and importance of anatomical form* (Ph.D. thesis), University of Bristol.
Gralton, J., Tovey, E., McLaws, M.-L., & Rawlinson, W. D. (2011). The role of particle size in aerosolised pathogen transmission: a review. *Journal of Infection*, *62*(1), 1–13.
Ingenia Industrial Design LLP 0000a. URL https://www.stl-tech.co.uk.
Innes, N., Johnson, I., Al-Yaseen, W., Harris, R., Jones, R., Kc, S., et al. (2021). A systematic review of droplet and aerosol generation in dentistry. *Journal of Dentistry*, *105*, Article 103556.
Juraeva, M., Park, B. H., Ryu, K. J., & Song, D. J. (2017). Designing high-speed dental air-turbine handpiece by using a computational approach. *International Journal of Precision Engineering and Manufacturing*, *18*, 1403–1407.
Liu, T., Nink, J., Merati, P., Tian, T., Li, Y., & Shieh, T. (2010). Deposition of micron liquid droplets on wall in impinging turbulent air jet. *Experiments in Fluids*, *48*, 1037–1057.
Liu, L., Wei, J., Li, Y., & Ooi, A. (2017). Evaporation and dispersion of respiratory droplets from coughing. *Indoor Air*, *27*(1), 179–190.
Lyaker, M., Al-Qudsi, O., & Kopanczyk, R. (2020). Looking beyond tracheal intubation: addition of negative airflow to a physical barrier prevents the spread of airborne particles. *Anaesthesia*, *75*(12), 1688–1689.
Mariam, Magar, A., Joshi, M., Rajagopal, P. S., Khan, A., Rao, M. M., et al. (2021). CFD simulation of the airborne transmission of COVID-19 vectors emitted during respiratory mechanisms: Revisiting the concept of safe distance. *ACS Omega*, *6*(26), 16876–16889.
Martinho, N., Lopes, A., & da Silva, M. G. (2012). Evaluation of errors on the CFD computation of air flow and heat transfer around the human body. *Building and Environment*, *58*, 58–69.
Matava, C. T., Yu, J., & Denning, S. (2020). Clear plastic drapes may be effective at limiting aerosolization and droplet spray during extubation: implications for COVID-19. *Canadian Journal of Anesthesia/Journal Canadien d'Anesthésie*, *67*, 902–904.
Menter, F. R. (1994). Two-equation eddy-viscosity turbulence models for engineering applications. *AIAA Journal*, *32*(8), 1598–1605.
Mutuku, J. K., Hou, W.-C., & Chen, W.-H. (2020). An overview of experiments and numerical simulations on airflow and aerosols deposition in human airways and the role of bioaerosol motion in COVID-19 transmission. *Aerosol and Air Quality Research*, *20*(6), 1172–1196.
Nishi, Y., Fushimi, H., Shimomura, K., & Hasegawa, T. (2018). Performance and internal flow of a dental air turbine handpiece. *International Journal of Rotating Machinery*, *2018*, 1–11.
Ong, S. J., Anil, G., Chia, K. L., Khoo, D., Lee, J. K., Chen, P. X., et al. (2022). The effectiveness of the Safety in Interventional Radiology (SIR) Shield in reducing droplet transmission and its effect on image quality and radiation dose. *The British Journal of Radiology*, *95*(1129), Article 20210835.
Organization, W. H. (2020). *Transmission of SARS-CoV-2: implications for infection prevention precautions: scientific brief, 09 July 2020*: *Technical documents*, (p. 10 p.). World Health Organization.
Organization, W. H., et al. (2014). *Infection prevention and control of epidemic-and pandemic-prone acute respiratory infections in health care*. World Health Organization.
Perella, P., Tabarra, M., Hataysal, E., Pournasr, A., & Renfrew, I. (2021). Minimising exposure to droplet and aerosolised pathogens: a computational fluid dynamics study. *British Journal of Anaesthesia*, *126*(2), 544–549.
Phu, H.-T., Park, Y., Andrews, A. J., Marabella, I., Abraham, A., Mimmack, R., et al. (2020). Design and evaluation of a portable negative pressure hood with HEPA filtration to protect health care workers treating patients with transmissible respiratory infections. *American Journal of Infection Control*, *48*(10), 1237–1243.
Pirker, L., Čebašek, M., Serdinšek, M., & Remškar, M. (2021). Size-and time-dependent aerosol removal from a protective box during simulated intubation and extubation procedures. *COVID*, *1*(1), 315–324.
Price, C., Ben-Yakov, M., Choi, J., Orchanian-Cheff, A., & Tawadrous, D. (2021). Barrier enclosure use during aerosol-generating medical procedures: A scoping review. *The American Journal of Emergency Medicine*, *41*, 209–218.
Rennie, C. E., Gouder, K. A., Taylor, D. J., Tolley, N. S., Schroter, R. C., & Doorly, D. J. (2011). Nasal inspiratory flow: at rest and sniffing. *International Forum of Allergy & Rhinology*, *1*(2), 128–135.
Schiller, V. L. (1933). Uber die grundlegenden berechnungen bei der schwerkraftaufbereitung. *Zeitschrift des Vereines Deutscher Ingenieure*, *77*, 318–321.
Sergis, A., Wade, W., Gallagher, J., Morrell, A., Patel, S., Dickinson, C., et al. (2021). Mechanisms of atomization from rotary dental instruments and its mitigation. *Journal of Dental Research*, *100*(3), 261–267.
Setti, L., Passarini, F., De Gennaro, G., Barbieri, P., Perrone, M. G., Borelli, M., et al. (2020). Airborne transmission route of COVID-19: why 2 meters/6 feet of inter-personal distance could not be enough. *International Journal of Environmental Research and Public Health*, *17*(8), 2932.
STL-Tech 0000b. URL https://www.stl-tech.co.uk.
Talaat, K., Abuhegazy, M., Mahfoze, O. A., Anderoglu, O., & Poroseva, S. V. (2021). Simulation of aerosol transmission on a boeing 737 airplane with intervention measures for COVID-19 mitigation. *Physics of Fluids*, *33*(3).
Tanabe, S., Kobayashi, K., Nakano, J., Ozeki, Y., & Konishi, M. (2002). Evaluation of thermal comfort using combined multi-node thermoregulation (65MN) and radiation models and computational fluid dynamics (CFD). *Energy and Buildings*, *34*(6), 637–646.
Tartarini, F., Schiavon, S., Cheung, T., & Hoyt, T. (2020). CBE Thermal Comfort Tool: Online tool for thermal comfort calculations and visualizations. *SoftwareX*, *12*, Article 100563. http://dx.doi.org/10.1016/j.softx.2020.100563, URL https://www.sciencedirect.com/science/article/pii/S2352711020302454.